

Deep Learning Exotic Hadrons

L. Ng,^{1,*} L. Bibrzycki,^{2,†} J. Nys,^{3,‡} C. Fernández-Ramírez,^{4,5,§} A. Pilloni,^{6,7,8,¶}
 V. Mathieu,^{9,10} A. J. Rasmusson,¹¹ and A. P. Szczepaniak^{11,12,13}

(Joint Physics Analysis Center)

¹*Department of Physics, Florida State University, Tallahassee, FL 32306, USA*

²*Pedagogical University of Krakow, 30-084 Kraków, Poland*

³*Institute of Physics, Ecole Polytechnique Fédérale de Lausanne (EPFL), CH-1015 Lausanne, Switzerland*

⁴*Departamento de Física Interdisciplinar, Universidad Nacional de Educación a Distancia (UNED), Madrid E-28040, Spain*

⁵*Instituto de Ciencias Nucleares, Universidad Nacional Autónoma de México, Ciudad de México 04510, Mexico*

⁶*Dipartimento di Scienze Matematiche e Informatiche, Scienze Fisiche e Scienze della Terra, Università degli Studi di Messina, Messina, I-98166, Italy*

⁷*INFN Sezione di Catania, Catania, I-95123, Italy*

⁸*INFN Sezione di Roma, Roma, I-00185, Italy*

⁹*Departament de Física Quàntica i Astrofísica and Institut de Ciències del Cosmos, Universitat de Barcelona, Martí i Franquès 1, E08028, Spain*

¹⁰*Departamento de Física Teórica, Universidad Complutense de Madrid and IPARCOS, E-28040 Madrid, Spain*

¹¹*Department of Physics, Indiana University, Bloomington, IN 47405, USA*

¹²*Theory Center, Thomas Jefferson National Accelerator Facility, Newport News, VA 23606, USA*

¹³*Center for Exploration of Energy and Matter, Indiana University, Bloomington, IN 47403, USA*

(Dated: May 18, 2022)

We perform the first amplitude analysis of experimental data using Deep Neural Networks to determine the nature of an exotic hadron. Specifically, we study the line shape of the $P_c(4312)$ signal reported by the LHCb collaboration and we find that its most likely interpretation is that of a virtual state. This method can be applied to other near-threshold resonance candidates.

Introduction.— Many hadron candidates that deviate from the quark model expectations [1] have been discovered in the last years [2, 3]. The field of hadron spectroscopy has flourished attempting to provide a comprehensive picture of the new states. Many different approaches have been proposed to explain their underlying nature, becoming a playground for testing new techniques and novel physical interpretations [4–7].

To determine if an experimental signal corresponds to a hadron resonance, it is necessary to perform an amplitude analysis in order to extract its physical properties such as mass, width, couplings, and quantum numbers. Most of the data analyses follow a top-down approach, where the amplitudes are derived from a microscopic model. The advantage is that it assigns a physical interpretation to the signal. The caveat is that the results are biased by the assumed dynamics. Another possibility is to proceed bottom-up. By considering a number of minimally-biased amplitudes compatible with physical principles and fitting them to data, one can determine the existence and properties of resonances in the least model-dependent way. Even though in this approach there is no assumed microscopic model it is still possible to deduce the nature of the underlying dynamics from the analytic properties of the amplitudes.

For example, both methods were recently used to provide an interpretation of the $P_c(4312)$ signal found by LHCb in the $\Lambda_b^0 \rightarrow K^- J/\psi p$ decay [8]. This measurement is of particular interest because, if due to a resonance, it would contain five valence quarks, which is beyond the baryon lore. The signal peaks approximately 5 MeV below the $\Sigma_c^+ \bar{D}^0$ threshold, making it a primary candidate for a hadron molecule. Near-threshold enhancements of the cross section are known phenomena in particle physics, *e.g.* the weakly-bound deuteron in proton-neutron scattering. The molecular interpretation was found to be compatible with the data in [9]. Another microscopic interpretation is that the signal is a kinematical effect generated by particle rescattering [10]. The $P_c(4312)$ pole position was first obtained in [11] following a bottom-up approach, favoring a virtual state interpretation, *i.e.* an attractive interaction that is not strong enough to bind a state, as it happens, for example, in neutron-neutron scattering [12].

The evolution of computing capabilities during the last decades has allowed to develop and employ powerful numerical techniques to unravel the structure of matter, with machine learning acquiring a prominent role. In theoretical hadron physics, techniques such as genetic algorithms [13] and neural networks [14] have been exploited as fitters and/or interpolators. Recently, the idea of using deep neural networks (DNN) as model classifiers was benchmarked against the well-known nucleon-nucleon bound state [15] and pion-nucleon resonances [16].

In this work we develop and benchmark a systematic approach to apply DNN as a model-independent tool to analyze and interpret experimental data. Following the

* ln16@my.fsu.edu

† lukasz.bibrzycki@up.krakow.pl

‡ jannes.nys@epfl.ch

§ cesar@jlab.org

¶ alessandro.pilloni@unime.it

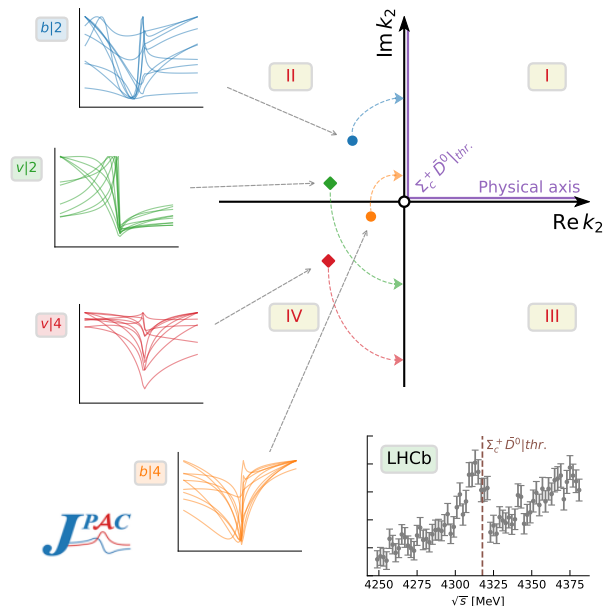


FIG. 1: Analytic structure of the amplitude near the $\Sigma_c^+ \bar{D}^0$ threshold. The adjacent Riemann sheets are continuously connected along the axes. The four possible resonant pole structures, that correspond to the classification classes, are depicted together with example line shapes. When the $J/\psi p$ and $\Sigma_c^+ \bar{D}^0$ channels decouple, the poles move to the imaginary k_2 axis along paths by the arrows. Poles moving to the positive (negative) axis correspond to bound (virtual) states. The bottom-right inset shows the data from LHCb in the $P_c(4312)$ region. The layout of the figure is inspired by [17].

bottom-up strategy, we construct generic amplitudes to train the DNN. We then use it as a model classifier to infer the physical content of the data. One clear advantage compared to standard χ^2 fits is that DNN determine the probability of each physical interpretation, as they learn the subtle classification boundary between them. We teach DNN how to recognize these different phases by targeting the specific regions of the parameter space (which yield stable solutions) that might be difficult to reach during optimization, or might require high resolution spectra to detect. The result of this is that we no longer need to explore large parameter spaces, but can use DNN to efficiently extract information from the spectra that determines on which side of the boundary we are located. As proof of concept, we apply this method to the $P_c(4312)$ signal.

Physics basis for the neural network.— We focus on the $J/\psi p$ invariant mass distribution reported by LHCb in [8]. This can be parametrized as [11, 18]

$$I(s) = \rho(s) [|P(s)T(s)|^2 + B(s)], \quad (1)$$

where s is the $J/\psi p$ invariant mass squared, $B(s)$ and

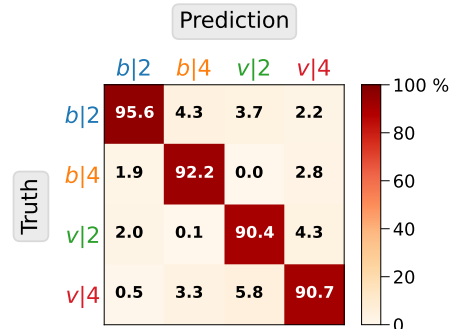
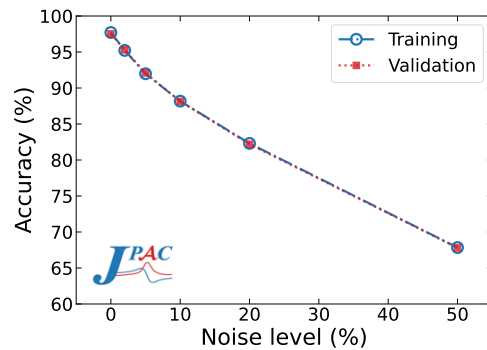


FIG. 2: (top panel) Accuracy as a function of the noise level σ of the training and validation datasets after 100 epochs in the [4.251, 4.379] GeV energy range. (bottom panel) Confusion matrix for the case of $\sigma = 5\%$. Percentages in the confusion matrix refer to the prediction accuracy.

$P(s)$ are smooth functions, and $\rho(s)$ the three-body phase space. The amplitude $T(s)$ encodes the dynamics of the $J/\psi p$ rescattering, and in particular contains the details of the $P_c(4312)$. Close to the $\Sigma_c^+ \bar{D}^0$ threshold, it can be expanded:

$$T(s) = \frac{m_{22} - ik_2}{(m_{11} - ik_1)(m_{22} - ik_2) - m_{12}^2}, \quad (2)$$

where $k_1 = \sqrt{s - (m_\psi + m_p)^2}$ and $k_2 = \sqrt{s - (m_{\Sigma_c^+} + m_{\bar{D}^0})^2}$. This Taylor expansion could originate from any microscopic model. The question is what is the range of validity. If other singularities closeby were present, the expansion would break down in this region. The impact of triangle singularities was estimated to be small in [8], and so was the relevance of higher order terms in the expansion [11]. It should be noted though, that if other singularities were close enough to impact, the model that describes them could be included in the training set of the DNN. In this case we mean to benchmark the approach by comparing to the known result in [11] as described by Eq. (2).

This function can be analytically continued for complex values of s . Since the square roots are multi-valued, the amplitude maps onto four Riemann sheets, repre-

sented in Fig. 1. By construction, this amplitude has four poles in the complex s plane. Two of them are a conjugated pair that appears either on the II or IV sheet, close to the $\Sigma_c^+ \bar{D}^0$ threshold where the expansion holds. The other two poles lay far away from the region of interest and have no physical interpretation. The pole position and sheet affect the observed line shape. Since the Eq. (1) is based on an expansion around the $\Sigma_c^+ \bar{D}^0$ threshold, it is only reliable in its vicinity. We thus have to ensure that the DNN learns from the appropriate invariant mass window.

If $m_{12} \rightarrow 0$, the $\Sigma_c^+ \bar{D}^0$ channel decouples from the $J/\psi p$ one. In this limit, the $P_c(4312)$ pole would become either a stable bound state, or a virtual threshold enhancement, depending on whether the pole would approach the positive or negative $\text{Im} k_2$ axis, as shown in Fig. 1. This is controlled by the sign of the m_{22} parameter: if it is positive (negative) the resonance corresponds to a virtual (bound) state. From the figure one can also appreciate that poles on the II (IV) sheet are more likely to be bound (virtual) states, as the sheet borders with the positive (negative) semiaxis.

We construct a training dataset of 10^5 line shapes, generated by evaluating Eq. (1) for intensity parameters uniformly sampled within a wide range of values (see Supplementary Material for details). We then obtain 65 intensity values by evaluating the line shape in the [4.251, 4.379] GeV invariant mass region in 2 MeV bins. The intensity line shapes were convoluted with the experimental resolution, and 5% Gaussian noise was added to the signal, to have statistical uncertainties that resemble the ones reported in Ref. [8]. An additional validation set is generated to monitor the generalization performance of the model during training. To each line shape, we attach a label according to the bound/virtual nature and the Riemann sheet where the pole lays, *i.e.* $b|2$, $b|4$, $v|2$, and $v|4$. Figure 1 shows examples of (noiseless) training line shapes for each class.

Training, validation, and invariant mass window.— We build a DNN using the PyTorch framework [19] that takes (noisy) line shapes as an input, and predicts the corresponding class $\{b|2, b|4, v|2, v|4\}$. For optimization purposes, the line shapes are first rescaled between 0 and 1 as a normalization before we feed them into the network. The DNN consists of an input layer with as many nodes as there are energy bins, followed by two fully-connected hidden layers with 400 and 200 nodes respectively, and finally an output layer with four nodes that correspond to the four classes. After each hidden layer we set a dropout probability that randomly sets nodes to zero, to improve generalization performance. The DNN is trained using the Adam optimizer [20]. The details of the procedure are given in the Supplemental Material. We train the DNN for 100 passes of the full training dataset through the DNN, *aka* epochs. Figure 2 shows the training and validation sets accuracy for different levels of Gaussian noise, as well as the confusion matrix for

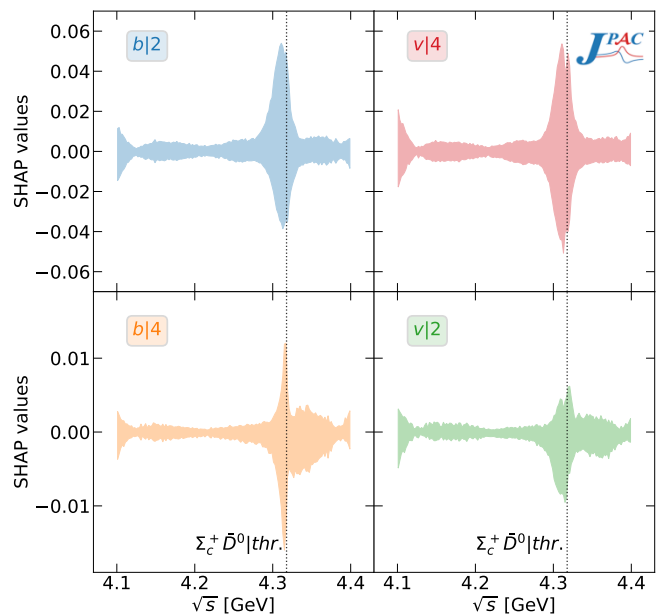


FIG. 3: Distribution of SHAP values as a function of the $J/\psi p$ invariant mass for the four classes for the training data with a 5% noise level. The shaded region corresponds to the 68% confidence level. The position of the $\Sigma_c^+ \bar{D}^0$ threshold is highlighted. It is apparent that such region has the largest impact. The amplification at the edges is a spurious border effect.

the case of 5% noise. This shows how the experimental uncertainty limits the accuracy, as expected. With this setup, the DNN learns the subtleties of the intensity line shapes associated with each one of the four different resonant pole structures. However, in order to obtain our final DNN classifier, we need to select the appropriate invariant mass window around the $P_c(4312)$ signal where we allow the DNN to attribute importance. We introduce a systematic method based on SHapley Additive exPlanations (SHAP) values [21] to select a proper window. Using SHAP values, we can break down a prediction to show how each bin impacts classification. Therefore, we train a first DNN to a wide range of invariant masses [4.1, 4.4] GeV. A positive (negative) SHAP value indicates that a given data point is pushing the DNN classification in favor (against) a given class. Large absolute SHAP values imply a large impact of a given mass bin on the classification, as shown in Fig. 3. The mass interval used here is the same as in [11]. This choice is confirmed by the SHAP values analysis shown in Fig. 3. However, we checked that the results are qualitatively unchanged even if a wider window is selected.

Signal analysis.— We are now in a position to generate predictions on the nature of the pole on the actual experimental LHCb data. We pass the three datasets from [8] through the DNN. We remind that one is the original $\Lambda_b^0 \rightarrow K^- J/\psi p$ dataset, while two have sharp or smooth

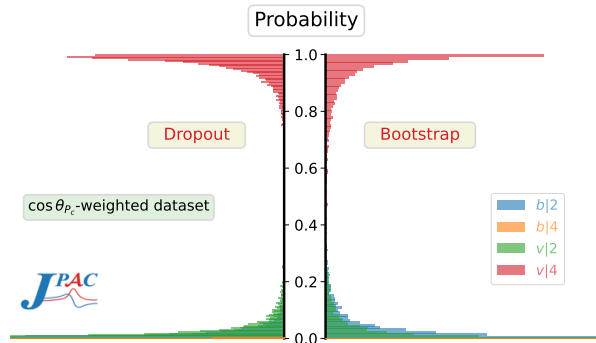


FIG. 4: Dropout and bootstrap classification probability densities for the predictions on $\cos \theta_{P_c}$ -weighted LHCb dataset, for each of the four classes. The $b|4$ (barely visible) and $v|2$ classes concentrate their probability density near zero. The x axis is cut for the purpose of visibility. The results for the other LHCb datasets are provided in the Supplemental Material.

TABLE I: Softmax output probabilities [22] for the three experimental datasets by LHCb [8].

	$b 2$	$b 4$	$v 2$	$v 4$
$\cos \theta_{P_c}$ -weighted	0.6%	< 0.01%	1.1%	98.3%
$m_{Kp} > 1.9$ GeV	1.4%	< 0.1%	1.6%	97.0%
m_{Kp} all	5.4%	< 0.1%	21.0%	73.6%

cuts that suppress the background from Λ^* resonances. The output probabilities for each class are summarized in Table I. It is apparent that the virtual interpretation is strongly favored, specifically the $v|4$ class. To properly quantify the uncertainty of this prediction, we use two Monte Carlo based methods: bootstrap [23, 24] and dropout [25]. Both methods aim at producing probability densities for the generated predictions on the LHCb data, as detailed in the Supplemental Material, and yield the same conclusions. The probability densities of the four classes are shown in Fig. 4. Class $v|4$ is heavily preferred, while $b|4$ is strongly rejected. Classes $b|2$ and $v|2$ attain low probabilities, in particular for the datasets with background rejection. Hence, we conclude that a virtual state with its pole placed on the IV Riemann sheet is the highly preferred interpretation of the $P_c(4312)$ signal.

The DNN classifier can provide further information on which invariant mass region contributes most strongly to this prediction, by repeating the SHAP analysis for the experimental data, as shown in Fig. 5. It is apparent how the region close to threshold determines the DNN classification. Slightly above threshold, data favor the $v|4$ class, while rejecting the $v|2$ one. Below threshold, the $v|4$ and $v|2$ classes are preferred to $b|2$, and $b|4$ is rejected.

Conclusions. — We presented a proof of concept of how

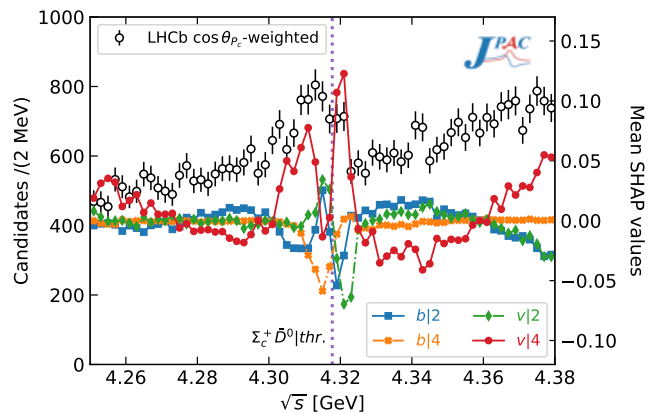


FIG. 5: $\cos \theta_{P_c}$ -weighted LHCb data (left axis) and distribution of their mean SHAP values (right axis) as a function of the $J/\psi p$ invariant mass for the four classes. The results for the other LHCb datasets are provided in the Supplemental Material.

machine learning can be used to further our understanding of exotic hadrons. We trained a neural network to learn the details of line shapes corresponding to different resonance interpretations, based on an effective range expansion of the amplitude close to the relevant threshold. We apply this method to determine the nature of the $P_c(4312)$ signal seen by LHCb. We determine the probability of each of the classes of interest, given the experimental uncertainties and resolution. A DNN classifier significantly favors a virtual state interpretation, *i.e.* generated by an attraction force not strong enough to form a bound state, thereby confirming the findings in Ref. [11]. By adding SHAP value analyses, we study how each data point impacts the selection. This technique also allows to assess which set of physical variables (in this case the energy range) is relevant to a specific hypothesis, which in standard approaches is often a heuristic guess. Our technique can be directly applied to other (non)exotic signals close to a threshold opening.

We foresee various followups. For example, one can reuse parts of DNN classifiers that generates line shape representations (*i.e.* parameters in the first layers), and reapply it to new data (so-called ‘transfer learning’) to obtain general resonance classifiers across scattering channels, and predict which physics underlies other reaction data.

ACKNOWLEDGMENTS

This work was triggered within the ‘‘Scattering theory and applications to hadrons’’ course taught under the Indiana University Global Classroom initiative. This work was supported by Polish Science Center (NCN) Grant No. 2018/29/B/ST2/02576, UNAM-PAPIIT Grant No. IN106921, CONACYT Grant No. A1-

S-21389, and U.S. Department of Energy Grants No. DE-AC05-06OR23177, No. DE-FG02-87ER40365, and DE-FG02-92ER40735. AP has received funding from the European Union's Horizon 2020 research and innovation programme under the Marie Skłodowska-Curie grant

agreement No. 754496. CFR is supported by Spanish Ministerio de Educación y Formación Profesional under Grant No. BG20/00133. VM is a Serra Hünter fellow and acknowledges support from the Spanish national Grants No. PID2019-106080 GB-C21 and No. PID2020-118758GB-I00.

-
- [1] M. Gell-Mann, *Phys.Lett.* **8**, 214 (1964); G. Zweig, *An SU(3) model for strong interaction symmetry and its breaking*, Tech. Rep. CERN-TH-401 (CERN, Geneva, Switzerland, 1964).
- [2] P. Zyla *et al.* (Particle Data Group), *PTEP* **2020**, 083C01 (2020).
- [3] S. L. Olsen, T. Skwarnicki, and D. Zieminska, *Rev.Mod.Phys.* **90**, 015003 (2018), arXiv:1708.04012 [hep-ph].
- [4] A. Esposito, A. Pilloni, and A. D. Polosa, *Phys.Rept.* **668**, 1 (2017), arXiv:1611.07920 [hep-ph]; A. Ali, L. Miani, and A. D. Polosa, *Multiquark Hadrons* (Cambridge University Press, 2019).
- [5] F.-K. Guo, C. Hanhart, U.-G. Meißner, Q. Wang, Q. Zhao, and B.-S. Zou, *Rev.Mod.Phys.* **90**, 015004 (2018), arXiv:1705.00141 [hep-ph].
- [6] F.-K. Guo, X.-H. Liu, and S. Sakai, *Prog.Part.Nucl.Phys.* **112**, 103757 (2020), arXiv:1912.07030 [hep-ph].
- [7] R. F. Lebed, R. E. Mitchell, and E. S. Swanson, *Prog.Part.Nucl.Phys.* **93**, 143 (2017), arXiv:1610.04528 [hep-ph]; M. Karliner, J. L. Rosner, and T. Skwarnicki, *Ann.Rev.Nucl.Part.Sci.* **68**, 17 (2018), arXiv:1711.10626 [hep-ph]; N. Brambilla, S. Eidelman, C. Hanhart, A. Nefediev, C.-P. Shen, C. E. Thomas, A. Vairo, and C.-Z. Yuan, *Phys.Rept.* **873**, 1 (2020), arXiv:1907.07583 [hep-ex].
- [8] R. Aaij *et al.* (LHCb), *Phys.Rev.Lett* **122**, 222001 (2019), arXiv:1904.03947 [hep-ex].
- [9] M.-L. Du, V. Baru, F.-K. Guo, C. Hanhart, U.-G. Meißner, J. A. Oller, and Q. Wang, *Phys.Rev.Lett.* **124**, 072001 (2020), arXiv:1910.11846 [hep-ph]; M.-L. Du, V. Baru, F.-K. Guo, C. Hanhart, U.-G. Meißner, J. A. Oller, and Q. Wang, *JHEP* **08**, 157, arXiv:2102.07159 [hep-ph].
- [10] S. X. Nakamura, *Phys.Rev.* **D103**, 111503 (2021), arXiv:2103.06817 [hep-ph].
- [11] C. Fernández-Ramírez, A. Pilloni, M. Albaladejo, A. Jackura, V. Mathieu, M. Mikhasenko, J. A. Silva-Castro, and A. P. Szczepaniak (JPAC), *Phys.Rev.Lett.* **123**, 092001 (2019), arXiv:1904.10021 [hep-ph].
- [12] H. W. Hammer and S. König, *Phys.Lett.* **B736**, 208 (2014), arXiv:1406.1359 [nucl-th].
- [13] D. G. Ireland, S. Janssen, and J. Ryckebusch, *Nucl.Phys.* **A740**, 147 (2004), arXiv:nucl-th/0312103 [nucl-th]; C. Fernández-Ramírez, E. Moya de Guerra, A. Udías, and J. M. Udías, *Phys.Rev.* **C77**, 065212 (2008), arXiv:0805.4178 [nucl-th]; R. D. Ball *et al.* (NNPDF), *JHEP* **04**, 040, arXiv:1410.8849 [hep-ph].
- [14] S. Forte, L. Garrido, J. I. Latorre, and A. Piccione, *JHEP* **05**, 062, arXiv:hep-ph/0204232; J. Rojo and J. I. Latorre, *JHEP* **01**, 055, arXiv:hep-ph/0401047; J. W. T. Keeble and A. Rios, *Phys.Lett.* **B809**, 135743 (2020), arXiv:1911.13092 [nucl-th]; C. Adams, G. Carleo, A. Lovato, and N. Rocco, *Phys.Rev.Lett.* **127**, 022502 (2021), arXiv:2007.14282 [nucl-th].
- [15] D. L. B. Sombillo, Y. Ikeda, T. Sato, and A. Hosaka, *Phys.Rev.* **D102**, 016024 (2020), arXiv:2003.10770 [hep-ph].
- [16] D. L. B. Sombillo, Y. Ikeda, T. Sato, and A. Hosaka, *Phys.Rev.* **D104**, 036001 (2021), arXiv:2105.04898 [hep-ph]; arXiv:2104.14182 [hep-ph] (2021).
- [17] J. J. Dudek, R. G. Edwards, and D. J. Wilson (Hadron Spectrum), *Phys.Rev.* **D93**, 094506 (2016), arXiv:1602.05122 [hep-ph].
- [18] W. R. Frazer and A. W. Hendry, *Phys.Rev.* **134**, B1307 (1964).
- [19] A. Paszke, S. Gross, F. Massa, A. Lerer, J. Bradbury, G. Chanan, T. Killeen, Z. Lin, N. Gimelshein, L. Antiga, A. Desmaison, A. Kopf, E. Yang, Z. DeVito, M. Raison, A. Tejani, S. Chilamkurthy, B. Steiner, L. Fang, J. Bai, and S. Chintala, in *Advances in Neural Information Processing Systems 32*, edited by H. Wallach, H. Larochelle, A. Beygelzimer, F. d'Alché-Buc, E. Fox, and R. Garnett (Curran Associates, Inc., 2019) pp. 8024–8035.
- [20] D. P. Kingma and J. Ba, in *3rd International Conference on Learning Representations, ICLR 2015, San Diego, CA, USA, May 7-9, 2015, Conference Track Proceedings*, edited by Y. Bengio and Y. LeCun (2015) arXiv:1412.6980 [cs.LG].
- [21] S. M. Lundberg and S.-I. Lee, in *Advances in Neural Information Processing Systems*, Vol. 30, edited by I. Guyon, U. V. Luxburg, S. Bengio, H. Wallach, R. Fergus, S. Vishwanathan, and R. Garnett (Curran Associates, Inc., 2017) arXiv:1705.07874 [cs.AI].
- [22] I. Goodfellow, Y. Bengio, and A. Courville, *Deep Learning* (MIT Press, 2016) <http://www.deeplearningbook.org>.
- [23] B. Efron and R. Tibshirani, *An Introduction to the Bootstrap*, Chapman & Hall/CRC Monographs on Statistics & Applied Probability (Taylor & Francis, 1994).
- [24] J. Landay, M. Döring, C. Fernández-Ramírez, B. Hu, and R. Molina, *Phys.Rev.* **C95**, 015203 (2017), arXiv:1610.07547 [nucl-th].
- [25] Y. Gal and Z. Ghahramani, in *Proceedings of The 33rd International Conference on Machine Learning*, Proceedings of Machine Learning Research, Vol. 48, edited by M. F. Balcan and K. Q. Weinberger (PMLR, New York, New York, USA, 2016) pp. 1050–1059, arXiv:1506.02142 [stat.ML].
- [26] K. Pearson, *The London, Edinburgh, and Dublin Philosophical Magazine and Journal of Science* **2**, 559 (1901).
- [27] J. Snoek, H. Larochelle, and R. P. Adams, in *Advances in Neural Information Processing Systems*, Vol. 25, edited by F. Pereira, C. J. C. Burges, L. Bottou, and K. Q. Weinberger (Curran Associates, Inc., 2012) arXiv:1206.2944 [stat.ML].

I. SUPPLEMENTAL MATERIAL

A. Theoretical intensity distribution

The intensity distribution is given by

$$I(s)_{\text{theo}} = \rho(s) [|F(s)|^2 + B(s)], \quad (3)$$

where

$$\rho(s) = m_{\Lambda_b} p q, \quad (4)$$

is the phase space factor with

$$p = \lambda^{1/2}(s, m_{\Lambda_b}^2, m_K^2)/2m_{\Lambda_b}, \quad q = \lambda^{1/2}(s, m_p^2, m_\psi^2)/2\sqrt{s}, \quad (5)$$

and $\lambda(x, y, z) = x^2 + y^2 + z^2 - 2xy - 2xz - 2yz$ is the Källén function. We assume that the $P_c(4312)$ signal has well-defined spin and contributes to a single partial wave. The background $B(s)$ is the smooth contribution from all other partial waves, which adds incoherently to the signal. Hence, we parametrize it as a first degree polynomial $B(s) = b_0 + b_1 s$. The amplitude $F(s)$ is the product of $P_1(s)$ and the $T_{11}(s)$ amplitude. $P_1(s)$ is also a smooth function that provides the production of $J/\psi p K^-$ and absorbs the cross channel Λ^* resonances projected onto the same partial wave as the $P_c(4312)$. We also parametrize it as a first degree polynomial $P_1(s) = p_0 + p_1 s$. $T_{11}(s)$ describes the $J/\psi p \rightarrow J/\psi p$ scattering. Hence, $F(s)$ can be written

$$F(s) = P_1(s) T_{11}(s), \quad (T^{-1})_{ij} = m_{ij} - ik_i \delta_{ij}, \quad (6)$$

where the m_{ij} are constants with $i, j = 1, 2$ corresponding to the $J/\psi p$ and the $\Sigma_c^+ \bar{D}^0$ channels, respectively. We define the momenta $k_1 = \sqrt{s - (m_\psi + m_p)^2}$ and $k_2 = \sqrt{s - (m_{\Sigma_c^+} + m_{\bar{D}^0})^2}$. Unitarity would prescribe the replacement of k_i by the two-body phase space. We approximated it by a square root alone, which is consistent with the effective range expansion near threshold, and with the nonrelativistic limit. The inclusion of the off-diagonal $P_2(s)T_{21}(s)$ term does not change the analytic properties of the amplitude and its effects can be absorbed into the parameters of $F(s)$. We stress that, since the $J/\psi p$ threshold is far away from the region of interest, this channel can effectively absorb all other channels with distant thresholds. Any contributions from further singularities are smooth in the region of interest and are effectively incorporated in the background parameters. For particle masses, we use the PDG values $m_{\Lambda_b} = 5.61960$ GeV, $m_p = 0.9382720813$ GeV, $m_K = 0.493677$ GeV, $m_\psi = 3.0969$ GeV, $m_{\bar{D}^0} = 1.86483$ GeV, and $m_{\Sigma_c^+} = 2.4529$ GeV [2]. The Σ_c^+ width has not been measured yet, but it is expected to be the same as its two isospin partners, $\Gamma_{\Sigma_c^0} = 1.83_{-0.19}^{+0.11}$ MeV and $1.89_{-0.18}^{+0.09}$ MeV. We neglect it, as it is similar to the experimental resolution.

B. Experimental energy resolution

The theoretical intensity is convoluted with the experimental resolution function

$$I(s) = \int_{m_\psi + m_p}^{m_{\Lambda_b} - m_K} I(s')_{\text{theo}} \exp\left[-\frac{(\sqrt{s} - \sqrt{s'})^2}{2R^2(s)}\right] d\sqrt{s'} \Big/ \int_{m_\psi + m_p}^{m_{\Lambda_b} - m_K} \exp\left[-\frac{(\sqrt{s} - \sqrt{s'})^2}{2R^2(s)}\right] d\sqrt{s'}, \quad (7)$$

where

$$R(s) = 2.71 \text{ MeV} - 6.56 \times 10^{-6} \text{ MeV}^{-1} \times (\sqrt{s} - 4567 \text{ MeV})^2 \quad (8)$$

is the experimental resolution provided by LHCb in [8].

C. Pole positions

To assign each pole a respective Riemann sheet location we need to find the roots of the denominator of Eq. (2) which in momentum space is equivalent to solving the following algebraic equation for $q = -ik_2$,

$$p_0 + p_1 q + p_2 q^2 + p_3 q^3 + q^4 = 0 \quad (9)$$

with

$$p_0 = (s_1 - s_2) m_{22}^2 - (m_{12}^2 - m_{11} m_{22})^2 \quad (10a)$$

$$p_1 = 2(s_1 - s_2) m_{22} + 2m_{11} (m_{12}^2 - m_{11} m_{22}) \quad (10b)$$

$$p_2 = -m_{11}^2 + m_{22}^2 + s_1 - s_2 \quad (10c)$$

$$p_3 = 2m_{22} \quad (10d)$$

where $s_1 = (m_\psi + m_p)^2$, $s_2 = (m_{D^0} + m_{\Sigma_c^+})^2$, which yields the poles in s solving $s = s_2 - q^2$. The poles appear in conjugate pairs, each on a sheet identified by (η_1, η_2) pair

$$\eta_1 = \text{Sign Re} \left(\frac{m_{12}^2}{m_{22} + q} - m_{11} \right) \quad \eta_2 = \text{Sign Re } q, \quad (11)$$

or by the customary naming scheme

$$\text{I sheet : } (+, +), \quad \text{II sheet : } (-, +), \quad (12a)$$

$$\text{III sheet : } (-, -), \quad \text{IV sheet : } (+, -). \quad (12b)$$

D. Dimensionality reduction and data visualization

In order to determine the location of the experimental $P_c(4312)$ mass spectrum, and whether it has support from the training data, we performed a Principal Component Analysis (PCA) to reduce the dimensionality [26]. PCA extracts the eigenvectors (Principal Components, PC) and eigenvalues of the training set's covariance matrix. The principal components are ordered by their normalized eigenvalues (which represent the explained variance) such that PC0 contains the largest fraction of dataset variance. Hereby, one can explain 99% of the variance of the training set by retaining 6 PCs. We show pairwise PC projections in Fig. 6 of the training and experimental data set. It can be seen that the LHCb data points are well encompassed by the training data in the reduced PCA space, suggesting that the amplitudes developed can describe the experimental data well. An additional PCA with 2 PCs (with 84.1% explained variance) is shown in Fig. 7, resulting in the same conclusion.

E. Neural Network Architecture

TABLE II: Detailed description of the architecture layers. All dense layers contain a bias term. We provide the shapes of the input and output tensors for a given batch size B, *i.e.* for an input batch of dimension (B, 65). See main text for details.

Layer	Shape in	Shape out
Input		(B, 65)
Dense	(B, 65)	(B, 400)
Dropout(p=0.2)	(B, 400)	(B, 400)
ReLU	(B, 400)	(B, 400)
Dense	(B, 400)	(B, 200)
Dropout(p=0.5)	(B, 200)	(B, 200)
ReLU	(B, 200)	(B, 200)
Dense	(B, 200)	(B, 4)
Softmax	(B, 4)	(B, 4)

A neural network is used in this study and is implemented in the PyTorch framework [19]. The architecture consists of two hidden layers with 400 and 200 nodes respectively. Rectified linear units (ReLU) are used as the activation function for these nodes [$\text{ReLU}(x) = \max(0, x)$]. After each of these hidden layers a dropout layer is included. This layer randomly masks nodes in a layer with a given probability, p . We use $p = 0.2$ and $p = 0.5$ for the first and second layer respectively. The final output layer consists of 4 nodes, each one representing a class. The softmax activation

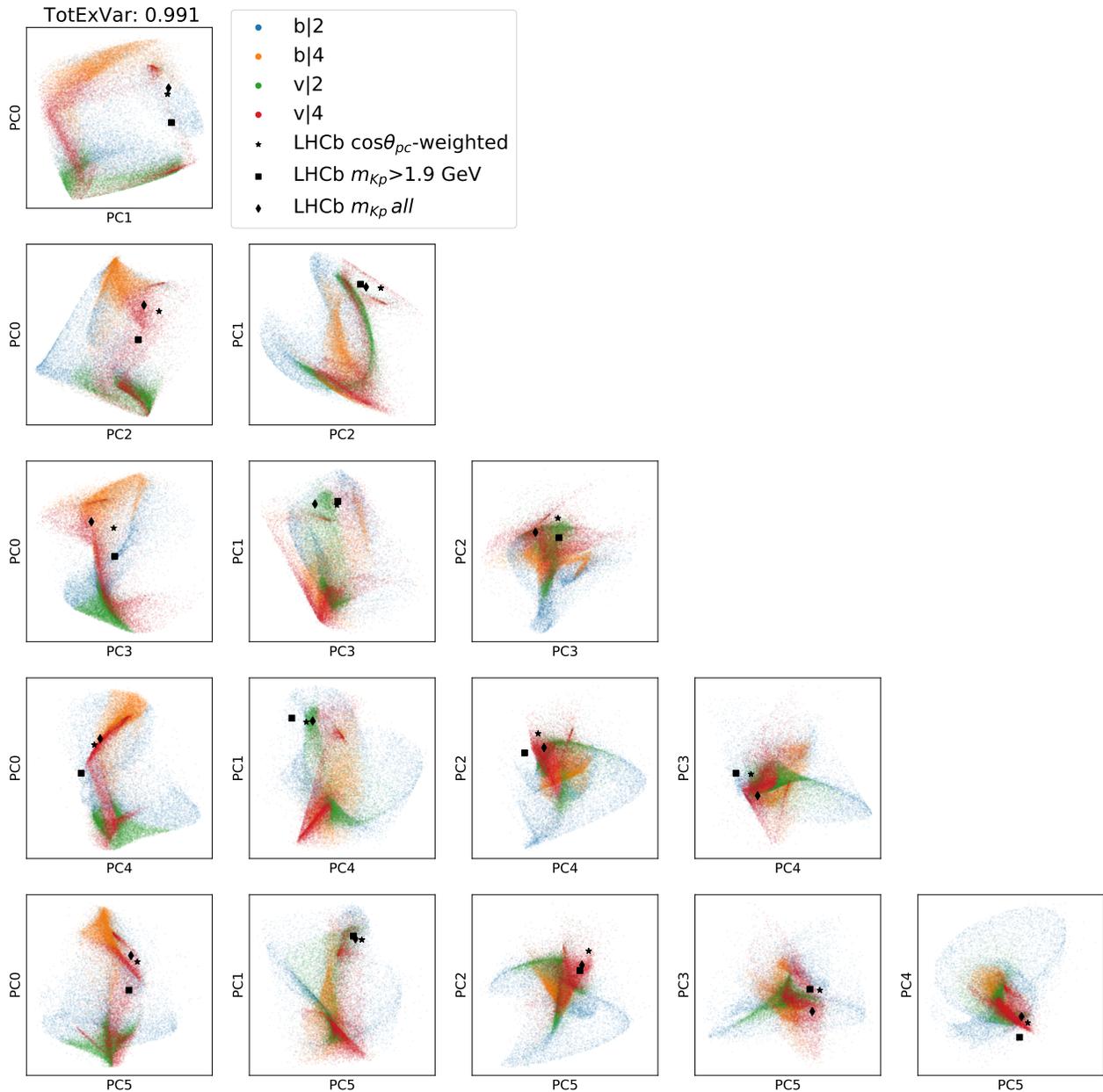


FIG. 6: Pairwise projections of training data samples onto the six principal components. Also shown are the projected three experimental LHCb datasets.

function is applied to the output of the final layer. This transformation is a generalization of the logistic function to multiple dimensions. For a vector $x = [x_1, \dots, x_C]^T$, with C the number of classes, the softmax function has the form [22]

$$\text{softmax}(x_i) = \frac{e^{x_i}}{\sum_j e^{x_j}}. \quad (13)$$

and allows the assignment of probabilities to each class. The network is optimized by minimizing the multi-class cross entropy loss. The architecture is tabulated in Table II. The Adam optimizer [20] is used with a learning rate of 0.001. The network is trained for 100 epochs with a batch size of 1024. Although the architecture was initially obtained through an educated guess, it was verified using Bayesian hyperparameter optimization [27], which found an optimum

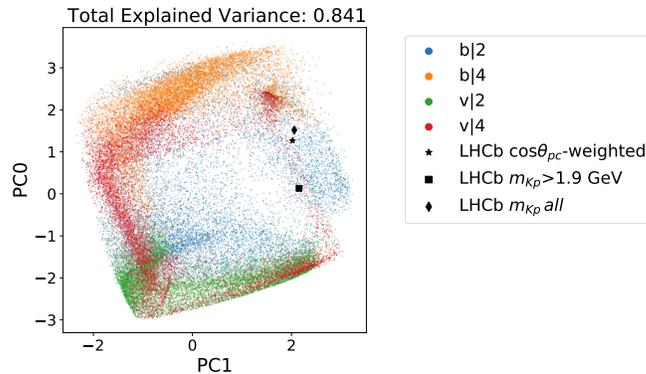


FIG. 7: Samples from the training data are projected onto a two-dimensional space using principal component analysis. The total explained variance in this two-dimensional projection is 0.841.

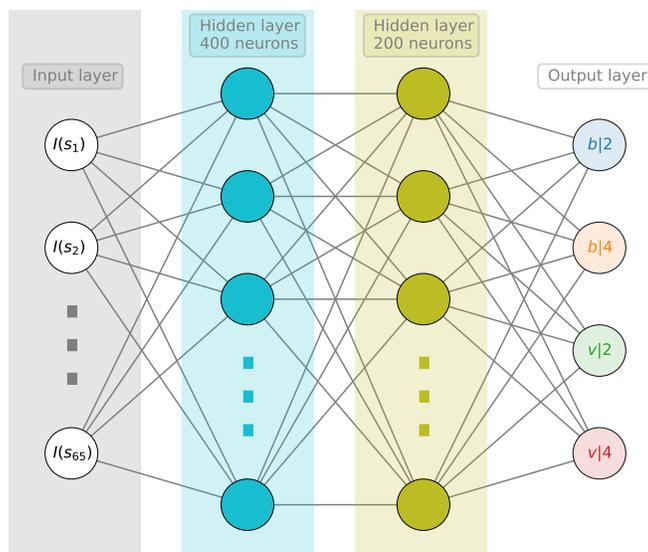


FIG. 8: Pictorial representation of the architecture of the DNN classifier with 65 input intensity points $I(s_n)$.

close to the figures cited above.

Figure 9 shows the evolution of the training and validation accuracy with the number of epochs. Multiple scenarios with varying noise levels are performed. Although the accuracy typically stabilizes after 40 epochs we let the DNN run up to 100 epochs. This result shows how the experimental uncertainty limits the accuracy, as expected.

F. Uncertainty Quantification

The effect of the experimental uncertainties in the classification needs to be properly quantified, so we can answer to the question on how strongly the prediction of our neural network depends on the instantiation of the statistical noise. We use two methods to extract uncertainties on the class predictions for the LHCb data. The bootstrap method uses 5000 samples of the LHCb data that are generated by sampling the LHCb data around its uncertainties, assuming the uncertainties are Gaussian. Then, the sampled data is passed through the network (without dropout). The second method (dropout, also known as Monte Carlo dropout) evaluates the model on the LHCb data (without error bars), but generates uncertainty distributions by sampling 5000 configurations for the dropout layers. Turning on

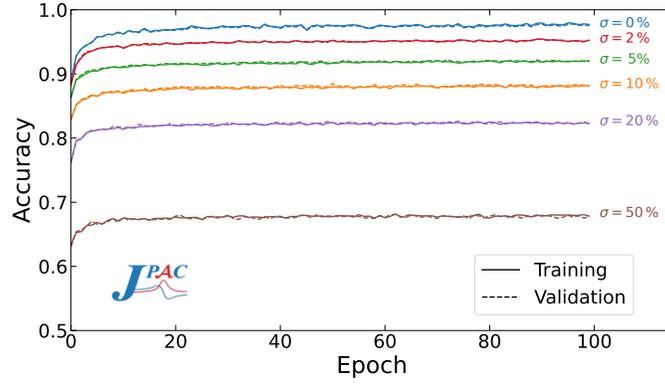


FIG. 9: Accuracy as a function of the epoch for the training and validation datasets in the $[4.251, 4.379]$ GeV energy range.

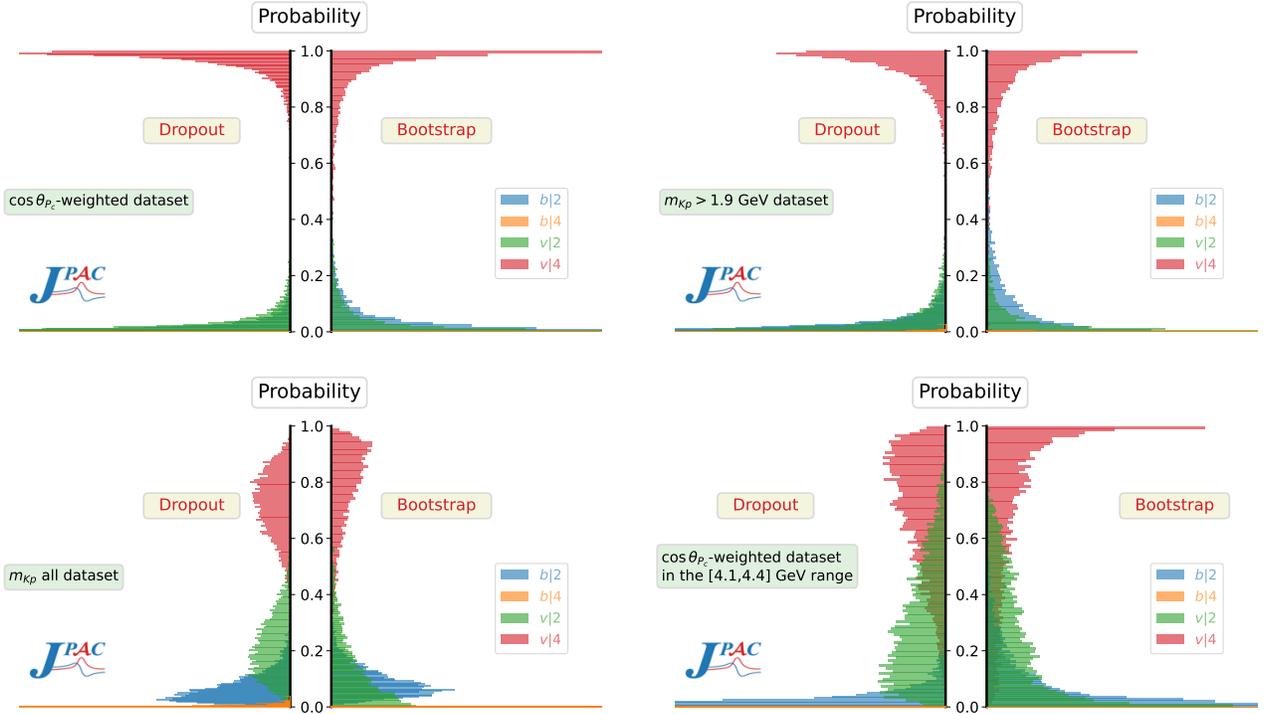


FIG. 10: Dropout and bootstrap classification probability densities for the predictions on the three LHCb datasets in the $[4.251, 4.379]$ GeV invariant mass range, and on the $\cos\theta_{P_c}$ -weighted on the $[4.1, 4.4]$ GeV range, for each of the four classes. The x axes are equally cut for the purpose of visibility and comparison.

dropout at evaluation time approximates Bayesian inference in a deep Gaussian process [25]. In Fig. 10 we show the resulting probability densities of the four classes and the three LHCb datasets in the $[4.251, 4.379]$ GeV range. For completeness, we also show the result for the $\cos\theta_{P_c}$ -weighted dataset for the wide $[4.1, 4.4]$ GeV range. This range covers datapoints far away from the region of interest and it is apparent how the virtual interpretation of the signal is still favored. Figure 11 shows the correlation of the probability densities obtained with both methods for the $\cos\theta_{P_c}$ -weighted dataset in the $[4.251, 4.379]$ GeV range.

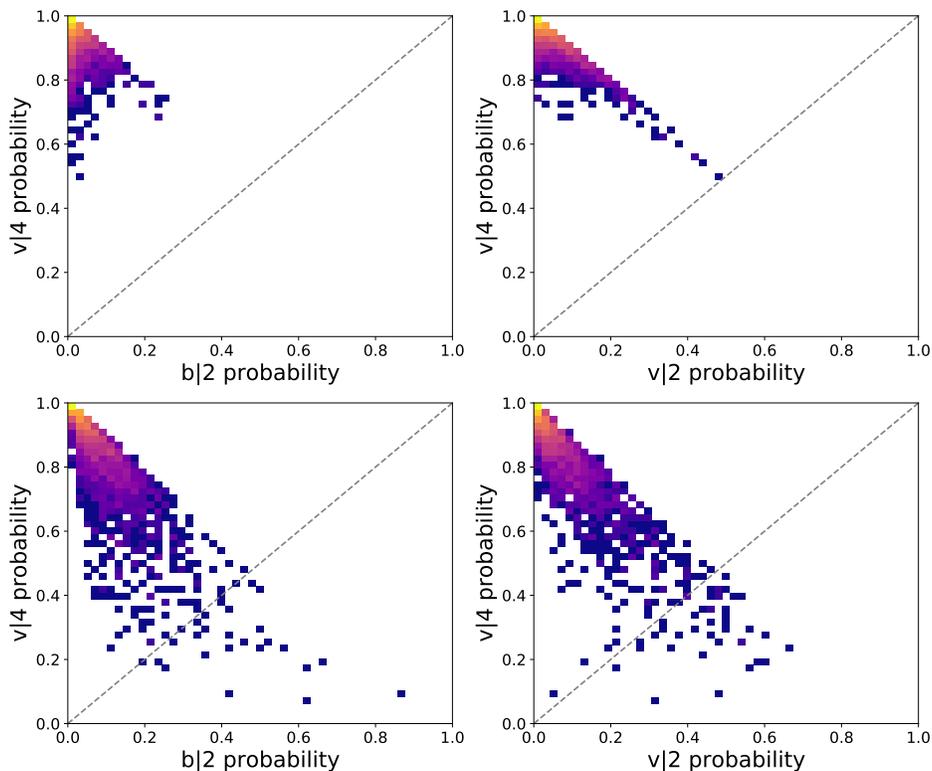


FIG. 11: Projections of the classification probability densities using dropout (top row) and bootstrap (bottom row) classification uncertainties with correlations for the $\cos\theta_{P_e}$ -weighted LHCb dataset in the $[4.251, 4.379]$ GeV range .

G. SHAP Values

SHapley Additive exPlanations (SHAP) values [21] allow to assess the impact of each datapoint in the prediction the DNN makes compared to a certain baseline. First we use them to validate the restricted invariant mass region used in the final analysis of the signal (See Fig. 3 of the manuscript), later we used them to quantify which class is favored by each experimental datapoint. Figure 12 shows the results for the three datasets reported by LHCb in [8]. In particular, we use the DeepExplainer implementation, which extracts approximate SHAP values [21]). The method is model agnostic and identifies the input contributions that lead to a certain prediction in a "fair" way. More specifically, the SHAP values represent the average marginal contribution of a feature (in our case, the datapoint at a certain invariant mass) over all feature coalitions (*i.e.* the whole set of considered datapoints). The marginal contribution is the difference in prediction with and without the feature. Each coalition represents a subset of the total feature dimensionality. DeepExplainer requires a background dataset to integrate over in order to extract approximate SHAP values. These SHAP values represent the difference in prediction between the background model output and the current model. A background dataset of 3000 spectra is taken and the SHAP values are computed for 1000 spectra.

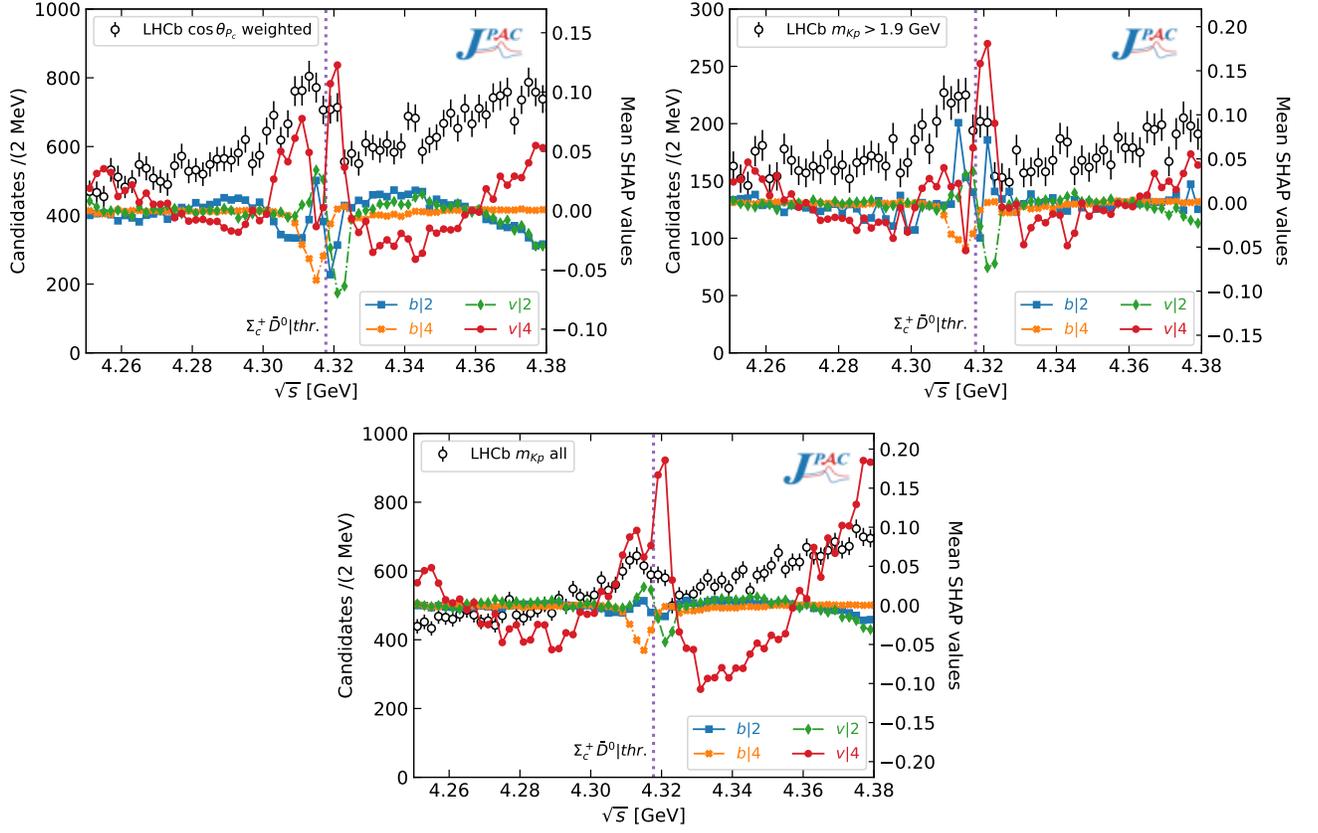


FIG. 12: LHCb data (left axis) and distribution of their mean SHAP values (right axis) as a function of the $J/\psi p$ invariant mass for the three LHCb datasets and the four classes.